Inorg. Chem. **2007**, *46*, 2299–2306

Phase Diagram of the $TbBr_3$–RbBr Binary System: Thermodynamic and Transport Properties of the Rb_3TbBr_6 Compound

Leszek Rycerz[†,‡] **and Marcelle Gaune-Escard***[,†]

Ecole Polytechnique Universitaire de Marseille, CNRS-UMR 6595, Technopole de Chateau Gombert, 5 rue Enrico Fermi, 13453 Marseille Cedex 13, France, and Chemical Metallurgy Group, Department of Chemistry, Wroclaw University of Technology, Wybrzeze Wyspianskiego 27, 50-370 Wroclaw, Poland

Received August 23, 2006

Phase equilibria in the $TbBr_3$–RbBr binary system were established from differential scanning calorimetry (DSC) measurements. This binary system is characterized by two compounds, namely Rb_3TbBr_6 and $RbTb_2Br_7$, and two eutectics located at the $TbBr_3$ mole fractions, $x = 0.117$ (728 K) and $x = 0.449$ (718 K), respectively. Rb_3TbBr_6 undergoes a solid–solid phase transition at 728 K and melts congruently at 1047 K with the related enthalpies 7.8 and 58.7 kJ mol^{-1}, respectively. $RbTb_2Br_7$ melts incongruently at 803 K. It undergoes also a solid–solid phase transition at 712 K, a temperature very close to that (718 K) of the second eutectic, and much attention was paid in evidencing and separating these transition and eutectic effects. Separate investigations of the thermodynamic and transport properties were performed on the Rb_3TbBr_6 compound. These heat capacity and electrical conductivity experimental results suggest an order–disorder mechanism in the alkali-metal cation sublattice whereas the $TbBr_6$ octahedra, forming the anionic sublattice, retain their normal lattice positions.

Introduction

In addition to their classical use for lanthanide metals and alloys production, the rare-earth halides receive an ever growing attention for recent technologies including pyrochemical fuel reprocessing in the nuclear industry. They are also attractive components in high-intensity discharge lamps[1,2] and new highly efficient light sources with energy saving features.[3−5] Finally, and more recently, they are subject to intensive research on optical devices. The study of upconversion (UC) phosphors has grown recently owing to their application in solid-state lasers,[6] optical fiber-based telecommunication,[7] illumination,[8] flat-panel displays and biological labeling,[9] and their ability to increase conversion efficiency in photovoltaic cells.[10] In particular, many rare-earth halide-based phosphors, as for instance, the fluoride-based precursors,[11−13] present upconversion abilities from infrared to visible light.

Assessment of their thermodynamic properties was conducted,[14] but even nearly 30 years after the documented review from Oak Ridge National Laboratory[15] on the anhydrous rare-earth halides and their binary systems with alkali-metal halides (mostly based on estimated values), it was also concluded that the properties of the rare-earth halides are poorly characterized and also that the bromides have received even less attraction than the chlorides and iodides.

* To whom correspondence should be addressed. E-mail: Marcelle.Gaune-Escard@polytech.univ-mrs.fr.
† Ecole Polytechnique.
‡ Wroclaw University of Technology.

(1) Elsam, L. E.; Preston, S. R. *Thermochim. Acta* **1992**, *205*, 319−21.
(2) Cordfunke, E. H. P.; Booij, A. S. *J. Chem. Thermodyn*. **1997**, *29*, 715−719.
(3) Guest, E. C.; Mucklejohn, S. A.; Preston, B.; Rouffet, J. B.; Zissis, G. *Proceedings of International Symposium on Ionic Liquids in Honour of M. Gaune-Escard*, Carry le Rouet, France, June 26−28, 2003; pp 37−45.
(4) Kirby, M. W. In *Lamps and Lighting*, 4th ed.; Coaton, J. R., Marsden, A. M.; Arnold: London, 1997; pp 227−234.
(5) Mucklejohn, S. A. *Proceedings of the International George Papatheodorou Symposium*, Patras, Greece, Sept 17−18, 1999; p 63.
(6) Downing, E.; Hhesselink, J.; Ralson, J.; MacFarlane, R. *Science* **1996**, *272*, 1185.
(7) Denjake, M. J.; Samson, B. *Mater. Res. Soc. Bull.* **1999**, 8, 39.
(8) Bergh, A. A.; Dean, P. *Light Emitting Diodes*; Clarendon Press: Oxford, U.K., 1976; p 343.
(9) Yi, G. S.; Lu, H. C.; Zhao, S. Y.; Ge, Y.; Yang, W. J.; Chen, D. P.; Guo, L. H. *Nano Lett.* **2004**, *4*, 2191.
(10) Millar, W. N.; Casida, L. E. *Can. J. Microbiol*. **1970**, *16*, 305.
(11) Wang, X.; Li, Y. *Angew. Chem., Int. Ed.* **2003**, *42*, 3497.
(12) Yan, R. X.; Li, Y. *Adv. Funct. Matter*. **2005**, *15*, 263.
(13) Zeng, J. H.; Su, J.; Li, Z. H.; Yan, R. X.; LI, Y. D. *Adv. Mater*. **2005**, *17*, 2118−2123.
(14) Mucklejohn, S. A.; Trindell, D. L.; Devonshire, R. Presented at the 6th International Symposium of Science and Technology Light Sources, Budapest, Hungary, 1992.
(15) Thoma, R. E. *Rare-Earth Halides*; ORNL-3804; 1965; pp 1−61.

10.1021/ic0615978 CCC: $37.00
Published on Web 02/21/2007

Therefore we initiated a general research program focused on lanthanide halides and their systems with alkali-metal halides. When this program was started, very little was known on $TbBr_3$ and only the enthalpy of formation at 298 K,[16] the melting temperature and enthalpy[17] were experimentally determined. No information was available in literature on terbium bromide−alkali-metal bromide systems. In this context, the thermodynamic properties of pure $TbBr_3$[18] and the phase diagrams of $TbBr_3$−NaBr[19] and $TbBr_3$−KBr[20] binary systems have been examined. The mixing enthalpies of $TbBr_3$−MBr liquid mixtures (M = Li, Na, K, Rb, Cs)[21] were also determined. This paper includes a phase diagram investigation of the $TbBr_3$−RbBr binary system. The congruently melting Rb_3TbBr_6 compound received particular attention, and thermodynamic and transport properties were determined.

Experimental Section

Sample Preparation. Terbium bromide, $TbBr_3$, was prepared by sintering bromination of terbium oxide, Tb_4O_7 (Johnson Matthey, 99.9%), with ammonium bromide, NH_4Br (POCh, Gliwice, Poland). The details of this synthesis and the chemical analysis of the product obtained have been described previously.[19]

Rubidium bromide was a Merck Suprapur reagent (minimum 99.9%). Prior to use, it was progressively heated to fusion under gaseous HBr atmosphere. HBr in excess was then removed from the melt by argon bubbling.

The mixtures of $TbBr_3$ and RbBr (in appropriate proportions) were melted in vacuum-sealed quartz ampules in an electric furnace. Melts were homogenized by shaking and solidified. These samples were ground with a pestle and an agate mortar in a glovebox. Homogeneous mixtures of different composition prepared along the same procedure were used in phase diagram measurements.

All chemicals were handled in an argon glovebox with a measured volume fraction of water of about 2×10^{-6} and continuous gas purification by forced recirculation through external molecular sieves.

Measurements. The temperatures and enthalpies of phase transitions of $TbBr_3$−RbBr binary mixtures were measured with a Setaram DSC 121 differential scanning calorimeter. The apparatus and the measurement procedure were described in detail previously.[22−23] Samples of 300−500 mg were contained in quartz ampules (about 6 mm diameter, 15 mm length) sealed under reduced pressure of argon. The sidewalls of ampules were grounded to fit the cells snugly into the heat flow detector. Experiments were conducted at heating and cooling rates ranging between 5 and 0.2 K min^{-1}.

Separate investigations were conducted on the Rb_3TbBr_6 compound. Heat capacity was measured with the same Setaram DSC 121 operated in a stepwise mode. In this so-called "step method", which has been already described,[23−26] the sample temperature is alternated in a series of heating and isothermal steps, the length of the isothermal steps being adjusted to allow sufficient time for reaching steady-state conditions. In the experimental heat flow plot against time, the area under each individual heating peak represents the heat required to increase the temperature at each step. The heat capacity of the sample was determined over an extended temperature range from two experimental series run in an identical stepwise mode, the first one with two empty cells (containers) of identical mass and the second with one of these cells loaded with the sample. For each heating step, the difference of heat flux between the two series is proportional to the amount of heat (Q_i) necessary to increase the sample temperature by a small temperature increment ΔT_i. Therefore, in the absence of any phase transition, the heat capacity of the sample is equal to

$$C_{p,m} = (Q_i M_s)/(\Delta T_i m_s) \quad (1)$$

where m_s is the mass of the sample and M_s is the molar mass of the sample.

The same operating conditions (i.e., initial and final temperatures, temperature increment, isothermal delay, and heating rate) were used in the two experimental series. Experimental monitoring, data acquisition, and processing were performed with the Setaram Setsys software.

The DSC 121 apparatus was calibrated by the Joule effect, and some test measurements were performed separately with NIST 720 α-Al_2O_3 standard reference material prior to investigation of the terbium bromide mixtures. These tests resulted in $C_{p,m}$ values consistent with standard data for Al_2O_3 (difference in all the temperature range less than 1.5%), which validated the step method use for heat capacity measurements. In the present heat capacity experiments each 5 K heating step was followed by a 400-s isothermal delay. The heating rate was 1.5 K min^{-1}. All experiments were performed in the 300−1100 K temperature range. The mass difference of the quartz cells in any individual experiment did not exceed 1 mg (cell mass: 400−500 mg).

Electrical conductivity measurements were carried out in a capillary quartz cell described in detail elsewhere.[27] The cell filled with the compound under investigation was placed into a furnace with a stainless steel block, used to achieve a uniform temperature distribution. The conductivity of the melt was measured by platinum electrodes with conductivity meter Radiometer CDM 230. Temperature was measured with a Pt/Pt−Rh thermocouple within an accuracy of 1 K. Temperature and conductivity data acquisition was made with a PC interfaced to the conductivity meter. Experimental runs were conducted both upon heating and cooling regimes at rates of 1 K min^{-1}. Experimental cells were calibrated at high temperature with a pure NaCl melt. All measurements were carried out under static argon atmosphere.

Results and Discussion

$TbBr_3$−RbBr Phase Diagram. The DSC investigations were performed on samples with 25 compositions, and the corresponding thermograms yielded both the temperatures and the enthalpy changes of the thermal events in the related mixtures. Enthalpy values of thermal effects obtained from

(16) Cordfunke, E. H. P.; Konings, R. J. M. *Thermochim. Acta* **2001**, *375*, 17−50.
(17) Thoma, R. E. In *Progress in the Science and Technology of the Rare Earths*; Eyring, L, Ed.; Pergamon Press: New York, 1996; pp 90−122.
(18) Rycerz, L.; Gaune-Escard, M. *J. Chem. Eng. Data* **2004**, *49*, 1078−1081.
(19) Rycerz, L.; Cieślak-Golonka, M.; Ingier-Stocka, E.; Gaune-Escard, M. *J. Therm. Anal. Calorim.* **2003**, *72*, 231−239.
(20) Rycerz, L.; Gaune-Escard, M. *Z. Naturforsch.* **2004**, *59a*, 84−90.
(21) Rycerz, L.; Gaune-Escard, M. *Z. Naturforsch.* **2001**, *56a*, 859−864.
(22) Gaune-Escard, M.; Rycerz, L.; Szczepaniak, W.; Bogacz, A. *J. Alloys Compd.* **1994**, *204*, 193−196.
(23) Rycerz, L.; Ingier-Stocka, E.; Cieslak-Golonka, M.; Gaune-Escard, M. *J. Therm. Anal. Calorim.* **2003**, *72*, 241−251.
(24) Rycerz, L.; Gaune-Escard, M. *Z. Naturforsch.* **1999**, *54a*, 229−235.
(25) Gaune-Escard, M.; Bogacz, A.; Rycerz, L.; Szczepaniak, W. *J. Alloys Compd.* **1996**, *235*, 176−181.
(26) Rycerz, L.; Gaune-Escard, M. *Z. Naturforsch.* **2002**, *57a*, 79−84.
(27) Fouque, Y.; Gaune-Escard, M.; Szczepaniak, W.; Bogacz, A. *J. Chim. Phys.* **1978**, *75*, 360.

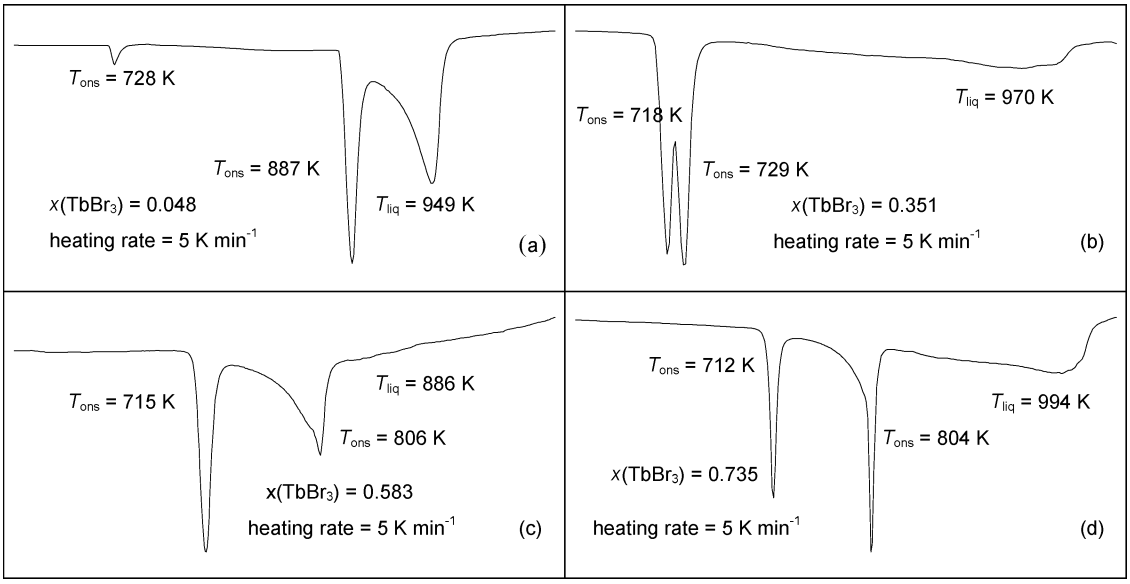

Figure 1. DSC heating curves for selected xTbBr$_3$−(1 − x)RbBr mixtures (x = 0.048, 0.351, 0.583, and 0.735).

heating and cooling runs were almost the same, the difference not exceeding 2%. However, supercooling was observed on cooling curves, and hence, the temperature and enthalpy data reported hereafter were taken from heating cycles only. Some characteristic DSC heating thermograms, corresponding to samples with the TbBr$_3$ molar fractions, x = 0.048, 0.351, 0.583, and 0.735, respectively (heating rate 5 K min^{-1}), are presented in Figure 1. In all these heating runs, the effect at the highest temperature corresponds to the liquidus temperature of each sample. The temperature of fusion of pure TbBr$_3$ (1103 K) was determined previously[18] by high-temperature Calvet microcalorimetry because of the temperature limitation of DSC.

In the composition range $0 < x < 0.250$, three endothermic peaks were present in all heating thermograms (Figure 1a, x = 0.048). The first one, at 728 K, was observable in all thermograms up to about x = 0.445, the composition at which it disappeared. The second one, at 887 K, only showed in those samples with composition $x < 0.250$, could be undoubtedly ascribed to the RbBr−Rb$_3$TbBr$_6$ eutectic effect. As quoted previously, the third effect corresponded to the liquidus temperature. The eutectic contribution to the enthalpy of fusion was determined and plotted against composition in Figure 2a.

This so-called Tamman construction made it possible to evaluate the eutectic composition accurately from the intercept of the two linear parts in Figure 2a, as x = 0.117. This RbBr−Rb$_3$TbBr$_6$ eutectic mixture melts with the enthalpy $\Delta_{fus}H_m \approx 16.0$ kJ mol^{-1}. In this Tamman construction it was assumed that there was no solubility in the solid state. Thus, the straight lines intercepted the composition axis at x = 0.0 and x = 0.250.

For the mixture of composition x = 0.250, only two effects were observed on thermograms. In addition to the effect at 728 K, the peak at 1047 K had a characteristic shape, typical of a congruently melting compound. From the above observations, we deduced the existence of the Rb$_3$TbBr$_6$ congruently melting compound in the TbBr$_3$−RbBr system, which undergoes a solid−solid phase transition at 728 K and melts congruently at 1047 K.

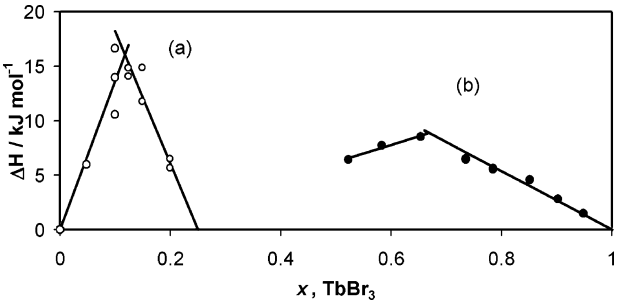

Figure 2. Determination of RbBr−Rb$_3$TbBr$_6$ eutectic (a) and RbTb$_2$Br$_7$ compound (b) compositions by a Tamman diagram: open circles, energetic effects related to the eutectic (x_{eut} = 0.117, T_{eut} = 887 K); black circles, effects related to the RbTb$_2$Br$_7$ decomposition (T_{dec} = 803 K); solid lines, linear regression of experimental results.

As observed with samples in the composition range $0 < x < 0.250$, three endothermic peaks were once again present in all heating thermograms in the composition range $0.666 < x < 1$ (Figure 1d, x = 0.735). As quoted previously, the effect at the highest temperature corresponds to the liquidus temperature. The thermal event at 803 K took place in all samples with $x > 0.522$ (Figure 1c,d). The enthalpy changes corresponding to this effect were plotted against composition in Figure 2b. This plot included two linear parts that intercepted at x = 0.669. This composition is consistent with the existence of the RbTb$_2$Br$_7$ compound. Thus, the thermal effect at 803 K can be ascribed to RbTb$_2$Br$_7$ incongruent melting, while the thermal event at 712 K should result from a solid−solid phase transition (or formation) of RbTb$_2$Br$_7$.

In the very narrow temperature range 712−728 K, several phase equilibria take place over the whole composition range. However, their number is difficult to appreciate over the composition range $0.250 < x < 0.666$. For this reason, we performed more detailed investigations on this composition

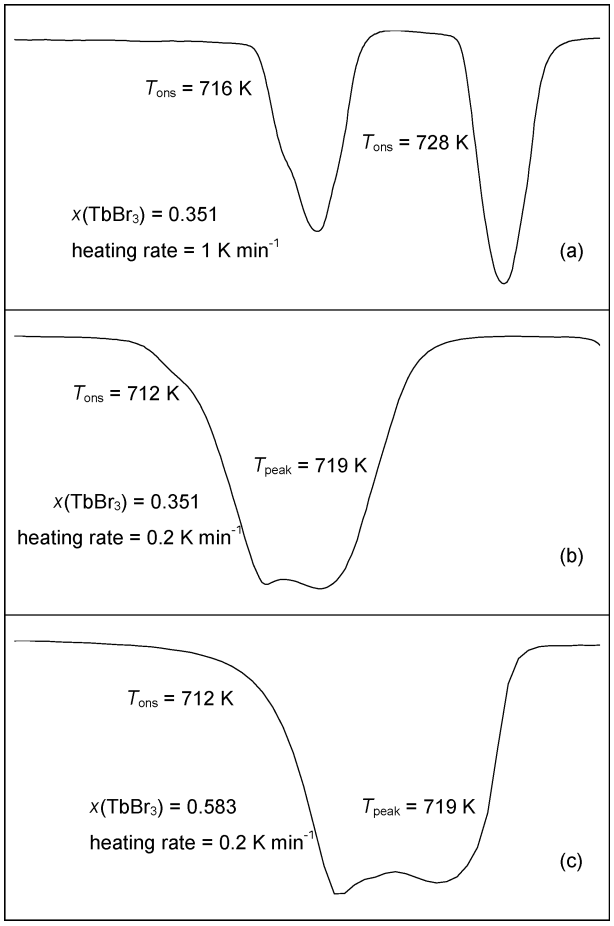

Figure 3. DSC heating curves for selected $x\mathrm{TbBr_3}-(1-x)\mathrm{RbBr}$ mixtures ($x = 0.351$ and 0.583).

range by running DSC scans at far smaller heating rates (1 and 0.2 K min^{-1}). Indeed the thermal events merged in Figure 1b,c were deconvoluted upon slower heating at 1 K min^{-1} (Figure 3a) and even revealed more details at 0.2 K min^{-1} (Figure 3b,c).

For mixtures in the composition range $0.250 < x < 0.445$, an additional effect at 718 K was visible in addition to the liquidus and Rb_3TbBr_6 transition at 728 K but merged with the latter under standard heating conditions (5 K min^{-1}). In an attempt to separate these events, further experimentation was performed at slower heating rates. While at 1 K min^{-1} the phase transition occurred separately, the anticipating effect at 718 K spited and could not be fully resolved even upon very slow heating (0.2 K min^{-1}), probably for kinetic reasons, as shown in Figure 3b.

However even so, two characteristic temperatures (712 and 719 K) were determined in all samples in the composition range $0.25 < x < 0.666$ and only one (712 K) at compositions beyond. As aforementioned, this temperature (712 K) was assigned to the solid−solid transition (or formation) of the $RbTb_2Br_7$ compound. Accordingly, the thermal event at 719 K should be related to the formation of a eutectic mixture of Rb_3TbBr_6 and $RbTb_2Br_7$.

The evaluation of this eutectic mixture composition from an enthalpy vs composition plot, as explained above, would not be reliable in view of the merged and nonseparable

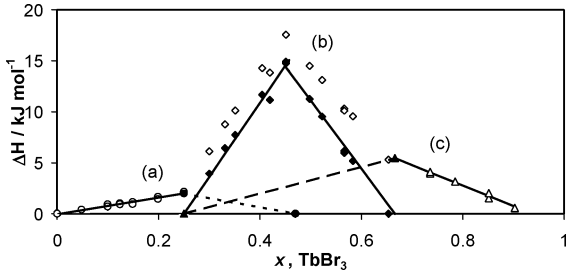

Figure 4. Graphical evaluation of the thermal effect related to the $Rb_3TbBr_6-RbTb_2Br_7$ eutectic: open circles, enthalpy related to the Rb_3TbBr_6 transition at 728 K (a); open triangles, enthalpy related to the $RbTb_2Br_7$ transition at 712 K (c); open diamonds, global enthalpy in composition range $0.25 \le x \le 0.666$; black diamonds, enthalpy related to the $Rb_3TbBr_6-RbTb_2Br_7$ eutectic with $T_{eut} = 718$ K (b).

enthalpy effects observed in the narrow temperature range 712−719 K. An alternate method was used instead.

The global enthalpy related to the overlapping effects, ΔH_m(global), was determined from DSC thermograms obtained at heating rate of 5 K min^{-1}. The enthalpy related to the eutectic, ΔH_m(eutectic), can be calculated as

$$\Delta H_m(\text{eutectic}) = \Delta H_m(\text{global}) - \Delta H_m(Rb_3TbBr_6\ \text{trans}) - \Delta H_m(RbTb_2Br_7\ \text{trans/form}) \quad (2)$$

The contribution of the enthalpy of transition, $\Delta H_m(Rb_3TbBr_6$ trans), to the global enthalpy could be determined from a Tamman diagram as shown in Figure 4a. The effect at 728 K only results from the solid−solid phase transition in Rb_3TbBr_6 at $x \le 0.25$, and the related enthalpy varies linearly with composition as

$$\Delta H_m(Rb_3TbBr_6\ \text{trans}) = 7.895x \quad (3)$$

with the maximal value 1.974 kJ mol^{-1} at $x = 0.25$. The linear dependence must occur also for $x > 0.25$. As the thermal effect related to this transition disappears at $x \sim 0.445$; thus, at $x = 0.445$ this enthalpy must be 0. Using the enthalpy values at $x = 0.25$ (1.974 kJ mol^{-1}) and $x = 0.445$ (0 kJ mol^{-1}) (black circles in Figure 4a) $\Delta H_m(Rb_3TbBr_6$ trans) was fitted to the linear equation ($0.25 \le x \le 0.445$)

$$\Delta H_m(Rb_3TbBr_6\ \text{trans}) = -8.973x + 4.217 \quad (4)$$

and plotted against x in Figure 4a (dashed line). The contribution of $\Delta H_m(RbTb_2Br_7$ trans/form) to the global enthalpy was described in a similar way (Figure 4c). The thermal effect at 712 K only results from the solid−solid phase transition (or formation) in $RbTb_2Br_7$ at $0.666 \le x < 1$. The corresponding enthalpy is a linear function of x:

$$\Delta H_m(RbTb_2Br_7\ \text{trans/form}) = -20.124x + 18.856 \quad (5)$$

Here there is the maximal value 5.453 kJ mol^{-1} at $x = 0.666$. The thermal effect related to this transition disappears at $x = 0.25$; thus, at $x = 0.25$ this enthalpy must be 0. The enthalpy values at $x = 0.25$ (0 kJ mol^{-1}) and $x = 0.666$ (5.453 kJ mol^{-1}) (black triangles in Figure 4c) resulted in the following equation of the $\Delta H_m(RbTb_2Br_7$ trans/form) in the molar fraction range $0.25 \le x \le 0.666$:

$$\Delta H_m(RbTb_2Br_7\ \text{trans/form}) = 13.108x - 3.277 \quad (6)$$

This is displayed in Figure 4c (broken line). By introducing eqs 4 and 6 into eq 2, it was then possible to calculate the enthalpy change related to the Rb_3TbBr_6−$RbTb_2Br_7$ eutectic (Figure 4b). The eutectic composition ($x = 0.449$) was determined from the intercept of the two linear parts in Figure 4b; the related fusion enthalpy $\Delta_{fus}H_m$ is about 14.5 kJ mol^{-1}. The detailed phase diagram of $TbBr_3$−RbBr binary system, resulting from these evaluations, is presented in Figure 5. Table 1 gives the temperatures corresponding to the different thermal events and the liquidus temperatures for all samples under investigation.

Thermodynamic and Transport Properties of the Rb_3TbBr_6 Compound. Rb_3TbBr_6 is the only congruently melting compound in the $TbBr_3$−RbBr binary system. As explained above it undergoes a solid−solid phase transition at 728 K and melts congruently at 1047 K with the related enthalpies 7.8 ± 0.2 and 58.7 ± 0.4 kJ mol^{-1}, respectively. Since no structural information was available in the literature regarding this compound, we made made conclusions about this solid−solid phase transition on the base of comparative studies for analogous chloride and bromide compounds.

M_3LnX_6 congruently melting compounds (M = K, Rb, Cs; Ln = lanthanide; X = Cl, Br, I) exist in almost all lanthanide halide−alkali-metal halide systems.[28−39] Systematic thermal, structural, and electrochemical measurements performed on chloride and $LaBr_3$−MBr systems[28−37] indicated that all the M_3LnX_6 compounds can be divided into two groups: compounds that are formed at high temperatures from M_2LnX_5 and MX, on the one hand, and compounds that exist at low temperatures as stable or metastable phases, on the other. Those compounds, which are formed at high temperatures, have only one, cubic, elpasolite-type, crystal structure. Their formation from M_2LnX_5 and MX is a reconstructive phase transition.[39] The other group of compounds existing at low temperatures have both low-temperature monoclinic, Cs_3BiCl_6-type and high-temperature cubic, elpasolite-type crystal structures.[28−37,39] The transition from low- to high-temperature modification is a nonreconstructive (displacive) phase transition.[39] We have measured

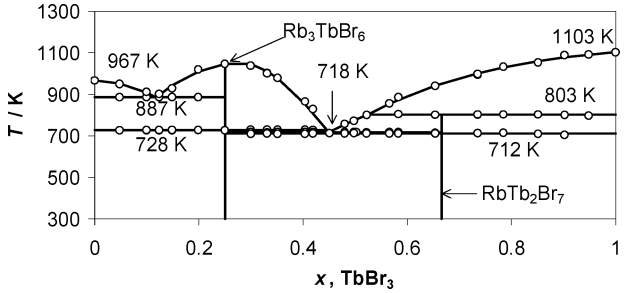

Figure 5. Phase diagram of the $TbBr_3$−RbBr binary system.

formation (or transition) enthalpies of a number of these compounds.[38,40−43] These results are presented in Table 2 together with literature information on crystal structures. They bring evidence that in the M_3LnX_6 compounds the large enthalpy effects (44−55 kJ mol^{-1}) are related to their formation from M_2LnX_5 and MX, while the modest enthalpy changes (6−9 kJ mol^{-1}) correspond to solid−solid phase transitions. It is thus reasonable to conclude that the thermal effect observed at 728 K in the Rb_3TbBr_6 compound with enthalpy of 7.8 kJ mol^{-1} is undoubtedly related to a solid−solid phase transition. By analogy with all the M_3LnX_6 compounds (Table 2), it can be assumed that Rb_3TbBr_6 has a monoclinic, Cs_3BiCl_6-type structure at low temperatures and cubic, elpasolite-type structure at high temperatures.

The heat capacity of the solid and liquid Rb_3TbBr_6 compound was experimentally determined at the temperature range 300−1100 K. These data were plotted against temperature in Figure 6 where, in accordance with the several thermal events evidenced in the previous section, several regimes are observed:

(1) Molar heat capacity of low-temperature modification varies smoothly with temperature up to about 650 K, at which temperature an unusual C_p rise anticipates the transition at 728 K.

(2) Heat capacity of high-temperature modification up to melting comprises two domains corresponding both to a linear C_p evolution with temperature, i.e. a nearly constant C_p; at about 885 K the well-visible heat capacity drop visualizes the change of regime.

(3) A constant value of heat capacity was found for the liquid phase.

In each temperature range, experimental data were least-square analyzed, and the corresponding $C_{p,m} = f(T)$ equations are reported in Table 3.

As mentioned above, the significant heat capacity increase of the Rb_3TbBr_6 low-temperature modification, with a characteristic λ-shape, thus suggesting a second-order transition, starts at about 650 K and is observed up to the phase transition temperature.

(28) Seifert, H. J.; Fink, H.; Thiel, G. *J. Less-Common Met.* **1985**, *110*, 139−147.
(29) Seifert, H. J.; Sandrock, J.; Thiel, G. *J. Therm. Anal.* **1986**, *31*, 1309−1318.
(30) Seifert, H. J.; Sandrock, J.; Uebach, J. *Z. Anorg. Allg. Chem.* **1987**, *555*, 143−153.
(31) Seifert, H. J.; Fink, H.; Uebach, J. *J. Therm. Anal.* **1988**, *33*, 625−632.
(32) Thiel, G.; Seifert, H. J. *Thermochim. Acta* **1988**, *133*, 275−282.
(33) Seifert, H. J.; Sandrock, J. *Z. Anorg. Allg. Chem.* **1990**, *587*, 110−118.
(34) Seifert, H. J.; Sandrock, J.; Thiel, G. *Z. Anorg. Allg. Chem.* **1991**, *598/599*, 307−318.
(35) Mitra, S.; Seifert, H. J. *J. Solid State Chem.* **1995**, *115*, 484−489.
(36) Zheng, Ch.; Seifert, H. J. *J. Solid State Chem.* **1998**, *135*, 127−131.
(37) Seifert, H. J.; Yuan, Y. *J. Less-Common Met.* **1991**, *171*, 135.
(38) Rycerz, L. *Thermochemistry of lanthanide halides and compounds formed in lanthanide halide-alkali metal halide systems*; Series Monograph 35; Scientific Papers of the Institute of Inorganic Chemistry and Metallurgy of Rare Elements; Wroclaw University of Technology: Wroclaw, Poland, 2004 (in Polish).
(39) Seifert, H. J. *J. Therm. Anal. Calorim.* **2002**, *7*, 789−826.
(40) Gaune-Escard, M.; Rycerz, L.; Szczepaniak, W.; Bogacz, A. *J. Alloys Compd.* **1994**, *204*, 189−192.
(41) Rycerz, L.; Gaune-Escard, M. *J. Thermal Anal. Calorim.* **1999**, *56*, 355−363.
(42) Rycerz, L.; Gaune-Escard, M. In *Progress in Molten Salt Chemistry 1, Prof. N. J. Bjerrum Special Volume*; Berg, R.E., Hjuler, H. A., Eds.; Elsevier: New York, 2000; pp 461−465.
(43) Rycerz, L.; Gaune-Escard, M. *J. Therm. Anal. Calorim.* **2002**, *68*, 973−981.

Table 1. Results of the DSC Experiments Performed on the $TbBr_3$−RbBr Binary System

x, $TbBr_3$	T_1/K for Rb_3TbBr_6 transition	T/K for $RbTb_2Br_7$ transition	T_3/K for eutectic RbBr−Rb_3TbBr_6	T_4/K for $RbTb_2Br_7$ dec	T_5/K for eutectic Rb_3TbBr_6−$RbTb_2Br_7$	$T_{liquidus}$/K
0.000						967
0.048	727		886			950
0.100	727		887			912
0.124	727		887			902
0.149	728		887			929
0.199	728		886			1020
0.250	727					1047
0.300	729	711			718	1038
0.331	730	712			716	1004
0.351	729	710			719	979
0.404	730	711			719	866
0.419	729	712			716	829
0.451		713			718	725
0.480		712			719	755
0.498		714			719	775
0.522		712		801	717	801
0.566		712		803	718	857
0.583		713		806	717	886
0.654		712		802	716	941
0.735		712		804		994
0.785		714		804		1033
0.851		710		804		1054
0.902		705		800		1089
0.948				798		1092
1.000						1103

Table 2. Crystal Structure and Molar Enthalpies of Formation or Transition of M_3LnX_6 Compounds

compd	cryst struct	$\Delta_{form}H_m$/kJ mol^{-1}	$\Delta_{trs}H_m$/kJ mol^{-1}	ref
K_3CeCl_6	H-temp, cubic, elpasolite-type[29]	55.4		40
K_3PrCl_6	H-temp, cubic, elpasolite-type[30]	52.6		40
K_3NdCl_6	H-temp, cubic, elpasolite-type[31]	46.3		40
Rb_3LaCl_6	H-temp, cubic, elpasolite-type[28]	48.4		40
Rb_3LaBr_6	H-temp, cubic, elpasolite-type[37]	44.0		41
K_3TbCl_6	L-temp, Cs_3BiCl_6-type; H-temp, cubic, elpasolite-type[35]		6.1	43
Rb_3PrCl_6	L-temp, Cs_3BiCl_6-type; H-temp, cubic, elpasolite-type[30]		6.6	40
Rb_3NdCl_6	L-temp, Cs_3BiCl_6-type; H-temp, cubic, elpasolite-type[31]		6.7	40
Rb_3TbCl_6	L-temp, Cs_3BiCl_6-type; H-temp, cubic, elpasolite-type[35]		7.6	43
Cs_3LaCl_6	L-temp, Cs_3BiCl_6-type; H-temp, cubic, elpasolite-type[28]		7.5	40
Cs_3CeCl_6	L-temp, Cs_3BiCl_6-type; H-temp, cubic, elpasolite-type[29]		7.8	40
Cs_3PrCl_6	L-temp, Cs_3BiCl_6-type; H-temp, cubic, elpasolite-type[30]		7.6	40
Cs_3NdCl_6	L-temp, Cs_3BiCl_6-type; H-temp, cubic, elpasolite-type[31]		7.4	40
Cs_3TbCl_6	L-temp, Cs_3BiCl_6-type; H-temp, cubic, elpasolite-type[35]		7.0	43
Cs_3LaBr_6	L-temp, Cs_3BiCl_6-type; H-temp, cubic, elpasolite-type[37]		9.0	41
Rb_3TbBr_6	L-temp, Cs_3BiCl_6-type?; H-temp, cubic, elpasolite-type?		7.8	this work

Very often such a transition is the result of disordering of mobile sublattice of solid electrolytes. Classical examples of ionic crystals undergoing a second-order phase transition indicate order−disorder transition in the cationic or anionic sublattice.[44] This disordering is reflected in the electrical conductivity of their solid phase.

Upon melting, the electrical conductivity of ionic salts generally increases strongly, typically by several orders of magnitude, up to a liquid value of about 10^2 S m^{-1}. Crystals with superionic or solid electrolyte phases, however, pass, either gradually or through a series of phase transitions, from normal ionic conductivity (less than 10^{-1} S m^{-1}) to liquidlike values while still solid.[45] It has occasionally been stated that the superionic phase results from "sublattice melting", that is, ions on a certain set of lattice positions become mobile,

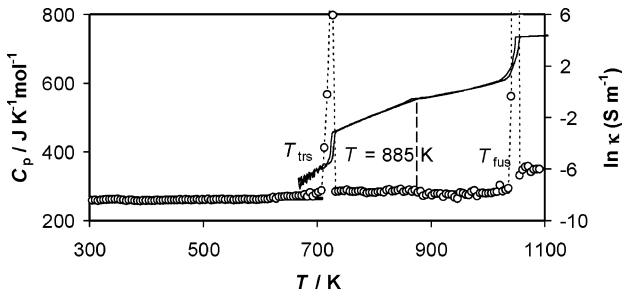

Figure 6. Molar heat capacity and ionic conductivity of Rb_3TbBr_6: open circles, experimental heat capacity; solid thick lines, polynomial fitting of experimental heat capacity data; solid thin lines, ionic conductivity.

Table 3. Molar Heat Capacity of Rb_3TbBr_6 Compound, $C_{p,m}$ (J mol^{-1}K^{-1}) = $a + bT$ (SE = Standard Error of Estimation)

compd	temp range/K	a/J mol^{-1} K^{-1}	10^2b/J mol^{-1} K^{-2}	SE/J mol^{-1} K^{-1}
Rb_3TbBr_6(s)	300−650	255.33	1.269	1.33
Rb_3TbBr_6(s)	737−885	285.99		1.90
Rb_3TbBr_6(s)	890−1035	279.72		5.90
Rb_3TbBr_6(l)	1060−1090	350.84		5.52

(44) Rickert, H. *Electrochemistry of Solids. An Introduction*; Springer-Verlag: Berlin, Heidelberg, Germany, New York, 1982; and references therein.

(45) Salamon, M.B. In *Topics in Current Physics, V. 15, Physics of Superionic Conductors*; Salamon, M. B., Ed.; Springer-Verlag: Berlin, Heidelberg, Germany, New York, 1979; and references therein.

almost liquidlike, while the remaining ions retain their normal lattice positions.[45] O'Keefe[45] divided ionic solids into three classes characterized by their phase transitions:

class I, "normally melting" salts such as alkali halides, which show large discontinuity in ionic conductivity at the melting point, with low conductivities and large activation energies in the solid state;

class II, crystals showing first-order solid electrolyte transitions;

class IIa, substances showing a large, discontinuous change in ionic conductivity and a change in the lattice symmetry of both mobile and nonmobile sublattices, typified by the $\alpha \rightarrow \beta$ transition in AgI;[44]

class IIb, crystals for which the changes in the immobile sublattice are minor;

class III, crystals in which the change from low to high ionic conductivity is spread over a wide temperature range and which have no change in the symmetry of the nonconducting sublattice.

CaF_2 and $SrCl_2$[36] for instance are prototype examples of class III.[44] Continuous disordering of one of their sublattice induces a characteristic behavior of other thermodynamic properties. The temperature range, where disordering starts to be high, corresponds to unusually high heat capacity values, consistent with the additional energy required by disorder increase. The dependence of heat capacity on temperature has a λ-shape and correlates well with electrical conductivity increase. The end of this λ-effect (complete structural disorder of sublattice) corresponds to a slope change of the electrical conductivity vs temperature plot.

The heat capacity features observed for Rb_3TbBr_6 may proceed from such an order−disorder mechanism, should its structure be compatible.

As said earlier, no structural information was available in literature regarding this compound. However, by analogy with all the M_3LnX_6 compounds (Table 2), it can be assumed that Rb_3TbBr_6 has a monoclinic Cs_3BiCl_6-type structure at low temperatures and cubic, elpasolite-type structure after the phase transition.

The latter structure was formally derived from the cubic elpasolite-type structure of A_2BMeX_6 compounds, in which the B and Me cations are octahedrally surrounded by 6 X^- ions, while the A cations are in a 12-fold environment.[46] This cubic structure is realized in the high-temperature modifications of the M_3LnX_6 compounds, which should be regarded as $M_2M'LnX_6$.[46]

A low-temperature, monoclinic Cs_3BiCl_6-type structure can be derived from the elpasolite-type, with LnX_6 octahedra slightly deformed markedly rotated from their ideal positions. These rotations reduce the difference in coordination between M and M′ cations. In the Cs_3BiCl_6 type structure one Cs ion is surrounded by 11 Cl ions and the other two are surrounded by 8 Cl ions. In both structures an anionic sublattice is formed by LnX_6 octahedra, whereas cations M and M′ form a cationic sublattice. With increase of temperature the alkali-metal cations become mobile, almost liquidlike, whereas LnX_6 octahedra retain their normal lattice positions.

(46) Seifert, H. J.; Fink, H. *J. Solid State Chem.* **1993**, *107*, 19.

Table 4. Activation Energies for Electrical Conductivity of the Rb_3TbBr_6 Compound

temp range/K	cryst struct	activatn energy/kJ mol^{-1}
670−725	monoclinc, Cs_3BiCl_6-type	128.5
773−885	cubic, elpasolite-type	94.0
885−1028	cubic, elpasolite-type	68.7
1055−1135	liquid phase	18.2

The high-temperature modification of Rb_3TbBr_6 is also derived from the elpasolite-type with 1/3 Rb and Tb cations octahedrally surrounded by Br ions and 2/3 Rb cations in a 12-fold environement.

Thus the only possible disordering in the Rb_3TbBr_6 lattice is the disordering of the cationic sublattice formed by rubidium cations. This disordering should be reflected in the electrical conductivity of the solid phase. To verify whether this disordering really occurs, electrical conductivity measurements were performed on the solid (and liquid) Rb_3TbBr_6 compound. The experimental results in the temperature range 670−1130 K are presented in Figure 6.

Specific electrical conductivity increases sharply with temperature (8.76×10^{-4} S m^{-1} at 670 K and 4.87×10^{-3} S m^{-1} at 725 K). Around 728−730 K a significant jump up to 3.71×10^{-2} S m^{-1} is observed. This jump is followed by a further global increase up to 2.47 S m^{-1} at 1028 K, while a change in the slope of electrical conductivity vs temperature plot is clearly observed at 885 K. A next conductivity jump occurs in the temperature range 1039−1055 K (from 4.14 S m^{-1} up to 71.19 S m^{-1}). From 1055 K, the conductivity of Rb_3TbBr_6 liquid phase is high. The corresponding activation energies for electrical conductivity are reported in Table 4.

In these four temperature ranges electrical conductivity obeys the classical Arrhenius equation. These results showed in particular that some changes occur in high-temperature modification, although no thermal event had been observed in DSC thermograms in this temperature range. Furthemore, in the $\ln \kappa$ vs T plot, the change of slope at about 885 K corresponds well to the unusual heat capacity decrease at that temperature (Figure 6).

For the low-temperature modification in the temperature range anticipating the phase transition, a correlated increase was evidenced for both electrical conductivity and heat capacity. This increase of electrical conductivity resulted from increase of current carrier ions number, proceeding by successive disordering of cationic sublattice formed by rubidium ions and also reflected in heat capacity evolution (Figure 6). Up to the solid−solid phase transition, Rb_3TbBr_6 features follow closely those of O'Keefe's class III solid electrolytes (continuous disordering). At the phase transition temperature, the jump in electrical conductivity corresponds to the heat capacity discontinuity—behavior characteristic of O'Keefe's class IIa (disordering induced by lattice symmetry change). After this phase transition, once again a typical class III behavior takes place. This global evolution suggests that cationic sublattice disordering in Rb_3TbBr_6 proceeds both continuously and discontinuously (phase transition). Starting at lower temperatures continuously up to the phase transition,

discontinuous disordering takes place at the temperature of phase transition. Then "complete disorder" is obtained at about 885 K in a continuous way (change of slope in electrical conductivity curve in Figure 6). In this "complete disorder" state rubidium cations are randomly distributed among $TbBr_6$ octahedra, which form the anionic sublattice.

IC0615978